## ORIGINAL ARTICLE

# Surface plasmon excitation in semitransparent inverted polymer photovoltaic devices and their applications as label-free optical sensors

Byoungchoo Park[1], Soo Hong Yun[1], Chan Youn Cho[1], Young Chan Kim[1], Jung Chul Shin[1], Hong Goo Jeon[1], Yoon Ho Huh[1], Inchan Hwang[2], Ku Youn Baik[1], Young In Lee[1], Han Sup Uhm[1], Guang Sup Cho[1] and Eun Ha Choi[1]

Herein, we report on surface plasmon (SP)-sensitive semitransparent inverted polymer photovoltaic (PV) devices that are based on multilayered material systems consisting of poly(3-hexylthiophene): fullerene-derivative bulk-heterojunction PV layers and thin gold or silver anodes. We demonstrate that these PV devices allow the simultaneous generation of both electrical power and SPs on their anodes for photoexcitation just above the optical absorption edge of the PV layers, resulting not only in attenuated total reflection, but also in attenuated photocurrent generation (APG) under the SP resonance (SPR) condition. Moreover, we also confirm that the biomolecular interaction of biotin–streptavidin on the PV devices can be precisely detected *via* apparent SPR angle shifts in the APG spectra, even without the need for complex attenuated total reflection configurations. We highlight our view that APG measurements made using these PV devices show great potential for the development of future generations of compact and highly sensitive SPR-based optical sensors.

## INTRODUCTION

The surface plasmon (SP) mode is a collective oscillation mode of electron density that is created at the boundary between a metal and a dielectric material; the SP mode can be excited at a metallic interface when the wavevector and frequency of plane-polarized incident light match those of the oscillation mode.[1–6] The resonant excitation of SP, otherwise known as SP resonance (SPR), has an extremely high level of sensitivity to the layer near the interface because its optical field can be confined and enhanced near the metallic surface.[1–6] This type of optical confinement and the enhancement of SPR are central to the development of new technologies in fields related to next-generation opto-electronic devices.[7–11]

One of the most promising SPR-based opto-electronic devices is the SP-enhanced photovoltaic (PV) device.[12–20] The SPR effect has been induced in several types of inorganic-[12–15] and organic-based[16–20] PV devices to improve the PV performance through the far-field light-scattering effect, near-field enhancement and/or enhanced exciton dissociation. These pioneering studies demonstrated that SPR is applicable to PV devices toward increasing the generation of photocurrent. The SPR effect was also recently introduced in highly efficient polymer-based PV devices (or bulk-heterojunction polymer solar cells (PSCs),[21–31] with power conversion efficiencies (PCEs), of 7%–10% or greater[23,24]) to demonstrate the potential of such devices.[32–38]

Among these, SP-enhanced inverted PSCs (IPSCs) with Au or Ag anodes show promise as efficient and long-term air-stable PV

devices.[36–38] In particular, due to the intrinsic optical properties of their Au or Ag layers,[1–6] SPR excitation in IPSCs may also facilitate the further enhancement of surface-sensitive opto-electronic performance levels. The enhanced performance of an IPSC can be applied to the development of new semiconducting devices and/or sensors. Furthermore, because of their simple structure and straightforward fabrication, SPR-active IPSC devices/sensors can also be used to broaden the areas of application of conventional label-free SPR sensors,[10,11] which have been used to understand chemical and biological interactions to obtain information regarding the kinetic processes of association and dissociation in real time, in addition to binding affinities and analyte concentrations. Therefore, there is a need to investigate systematically the excitation mechanisms of SPs at the interface inside IPSCs; such investigations may then guide the development of new SPR-based surface-sensitive opto-electronic devices and sensors.

Herein, we report our investigation of the excitation of the SP mode supported by a planar multilayer structure of a semitransparent inverted polymer PV device with a thin Au or Ag film anode. We show that the excitation of SPs on the IPSC, caused by incident light of appropriate wavelengths, results in significant attenuation not only in terms of the total internal reflection (attenuated TIR, hereafter ATR) of the incident light but also in terms of the PV performance *via* the generation of photocurrent (attenuated photocurrent generation, hereafter APG) in the PV device, thereby yielding the characteristics of SPR-sensitive polymer PV devices.

By means of proof-of-concept experiments, we show that the SPR-sensitive polymer PV devices act as optical detectors integrated into an SPR coupler and that the integrated functionality of these devices allows the sensitivity of the APG mode to be almost identical to that of the ATR mode for detecting SPR signals. Such an APG mode can be used to develop simple, compact, inexpensive, and highly surface-sensitive SPR sensors, thereby offering all of the benefits associated with the miniaturization of label-free SPR sensors for flexible and wide-ranging applications, as mentioned above.

## MATERIALS AND METHODS

To form a PV layer, we used poly(3-hexylthiophene) (P3HT, regioregularity: 93%, average molecular weight: 37 000; 1-Material, Dorval, QC, Canada) and phenyl $C_{61}$-butyric acid methyl ester (PCBM; Nano-C, Westwood, MA, USA). A blended solution was made by adding P3HT (2.40 wt-%) and PCBM (1.76 wt-%) to a solvent of 1,2-dichlorobenzene. To fabricate the semitransparent IPSC, an indium tin oxide (ITO, 80 nm, 30 $\Omega$ square$^{-1}$) layer on a glass substrate was used as the transparent cathode. After routine cleaning of the ITO substrate, an electron-collective interlayer composed of a mixture of poly(ethylene oxide) (PEO) and cesium carbonate ($Cs_2CO_3$) ($PEO:Cs_2CO_3=1.00:0.70$, thickness: approximately 10 nm)[30] was spin-coated on the ITO glass. Then, the blended solution of P3HT and PCBM was spin-coated on top of the $PEO:Cs_2CO_3$ interlayer and pre-annealed at 120 ℃ for 3 min to form a P3HT:PCBM PV layer approximately 220–230 nm thick.

After pre-annealing, an approximately 30-nm-thick molybdenum oxide ($MoO_3$; Sigma-Aldrich, St. Louis, MO, USA) layer was formed as a hole-collection interlayer on top of the P3HT:PCBM layer by thermal deposition (0.5 nm s$^{-1}$) at a base pressure less than $2.7\times10^{-4}$ Pa. A thin Au anode layer was then formed on the $MoO_3$ layer using sputter deposition (0.2 nm s$^{-1}$) in Ar at a base pressure less than $5\times10^{-1}$ Pa with a thickness of approximately 45 nm on the Au anode (approximately 3.6 $\Omega$ square$^{-1}$). After fabrication, the devices were annealed at 150 ℃ for 10 min to induce the crystallization of the PV layer.[27,30] Thus, the device structure consisted of the sequence (ITO/$PEO:Cs_2CO_3$/P3HT:PCBM/$MoO_3$/thin Au)(sample device, Au-IPSC). For comparative purposes, using the sequence (ITO/$PEO:Cs_2CO_3$/P3HT:PCBM/$MoO_3$/thin Ag) (sample device, Ag-IPSC), we also fabricated another set of IPSCs by the sputter deposition of a thin Ag anode (approximately 45 nm, 5.9 $\Omega$ square$^{-1}$).

The optical absorption and transmission/reflection properties of the functional layers used in the IPSCs were investigated using ultraviolet-visible spectrometers (Cary 1E UV-vis spectrometer; Varian Inc., Palo Alto, CA, USA). The PV performance of the fabricated IPSCs was measured under an illumination intensity of 100 mW cm$^{-2}$ generated by an AM 1.5G light source (96000 Solar Simulator; Newport, Irvine, CA, USA). The current density–voltage ($J$–$V$) characteristics were measured using a source meter (Keithley 2400; Keithley Instrument Inc., Cleveland, OH, USA) and calibrated using a reference cell (BS-520; Bunkoh-Keiki Co., Ltd., Otsuka, Tokyo, Japan). The incident photon-to-current collection efficiency (IPCE) spectra were measured using an IPCE measurement system.

For the ATR prism-coupling technique in the Kretschmann geometry,[4–6] the glass substrate of the Au-IPSC device was attached to a 45°–45°–90° BK7 coupling prism using index matching oil. We then investigated the excitation of SPs on the Au-IPSC assembly using the ATR coupling prism (Au-IPSC/prism) mounted on a rotating stage to control the angle of incidence $\theta$ of the incident light. The Au-IPSC/prism sample was then illuminated through the input facet of the prism with a transverse-magnetic-polarized (TM-polarized) monochromatic incident laser light of wavelength ($\lambda$) of 632.8 nm (beam diameter

approximately 0.81 mm) and an incident power of approximately 1.8 μW. An optical power meter mounted on a $\theta$–$2\theta$ rotating stage was used as the external photodetector for monitoring the reflectance ($R(\theta)$) from the Au-IPSC/prism sample. The optical setup was controlled by means of a stand-alone computer with software that enabled the angular spectra of $R(\theta)$ and $J_{SC}(\theta)$ to be recorded as a function of the incident angle $\theta$, which was increased in steps of 0.016°.

To form adlayers on the Au-IPSC, we used an amorphous perfluoropolymer, Cytop (Asahi Glass Co., Ltd., Amagasaki, Hyōgo, Japan), as a cladding buffer adlayer, and BSA (bovine serum albumin, #9048-46-8; Sigma-Aldrich) as a protein adlayer. To form the Cytop cladding buffer adlayer, we spin-coated a solution of Cytop on the Au anode of the Au-IPSC. To form bi-adlayers of Cytop/BSA, we also spin-coated a solution of BSA on the Cytop adlayer pre-coated on the Au anode of the IPSC. The BSA solution was made by adding BSA (0.4 wt-%) to a solvent of deionized (DI) water (pH=7). To desorb the bi-adlayers of Cytop/BSA, the bi-adlayer-coated Au-IPSC was treated using three successive cleaning processes: (i) washing with flowing DI water for 3 min; (ii) exposure to pure Ar atmospheric pressure (AP, 5 mL min$^{-1}$) plasma; and (iii) re-exposure to $Ar/O_2$ AP plasma (0.8% of $O_2$). To generate the AP plasma, we used a radiofrequency plasma generator under the glow discharge condition with a 13.56-MHz radiofrequency power supply (100 W).

To bind biomolecules to the Au-IPSC, we used biotinylated BSA (Bio-BSA, #B-2007; Vector Laboratories, Inc., Burlingame, CA, USA) as a model receptor and streptavidin (STA, #85878; Sigma-Aldrich) as a model analyte. First, a Cytop adlayer was spin-coated on the Au-IPSC (step 1). To form a molecular layer of Bio-BSA on the Cytop layer, 20 μL of Bio-BSA solution (1 μg mL$^{-1}$ in phosphate buffer saline) was deposited on the Cytop-coated Au anode of the Au-IPSC and then incubated at 25 ℃ for 5 min. The Bio-BSA-formed Au-IPSC was then rinsed three times with DI water and dried under a stream of $N_2$ (step 2).

Next, to bind the STA to the Bio-BSA layer, we used a solution (0.02 mg mL$^{-1}$ in phosphate buffer saline) of STA, which was diluted to various concentrations in phosphate buffer saline. The diluted solution (20 μL) of STA was deposited on the Bio-BSA-functionalized Au-IPSC and then incubated at 25 ℃ for 5 min. The incubated Au-IPSC was then rinsed three times with DI water and dried under a stream of $N_2$ (step 3). To confirm the biomolecular binding on Bio-BSA at steps 2 and 3, red fluorescent anti-biotin-Cy3 monoclonal antibody (C5585; Sigma-Aldrich) and green fluorescent fluorescein isothiocyanate-conjugated STA (S3762; Sigma-Aldrich) were used to visualize the molecular binding on a stripe-patterned Bio-BSA layer with a BSA-blocking layer on the Au-IPSC using a fluorescent microscope (Eclipse Ti–U; Nikon, Chiyoda-ku, Tokyo, Japan).

## RESULTS AND DISCUSSION

The schematic structure and energy diagrams of the semitransparent IPSCs used to achieve SP excitation with the appropriate energy level alignment are shown in Figure 1a and Supplementary Fig. S1a, respectively. As shown in Figure 1a, to observe the PV characteristics, either the ITO cathode side (bottom illumination) or the semitransparent Au or Ag anode side (top illumination) can be subjected to irradiation from a solar simulator, in view of the semitransparency of the fabricated IPSCs. Simultaneously, the thin Au or Ag anode also serves as a coupling layer for TM-polarized incident light to excite SPs on the device.[2–6] First, we investigated the optical properties of an IPSC fabricated using a thin Au anode (Au-IPSC), finding that the Au-IPSC exhibited strong optical absorption with a peak at approximately 495–510 nm, mainly attributed to the $\pi$–$\pi^*$ transition of the
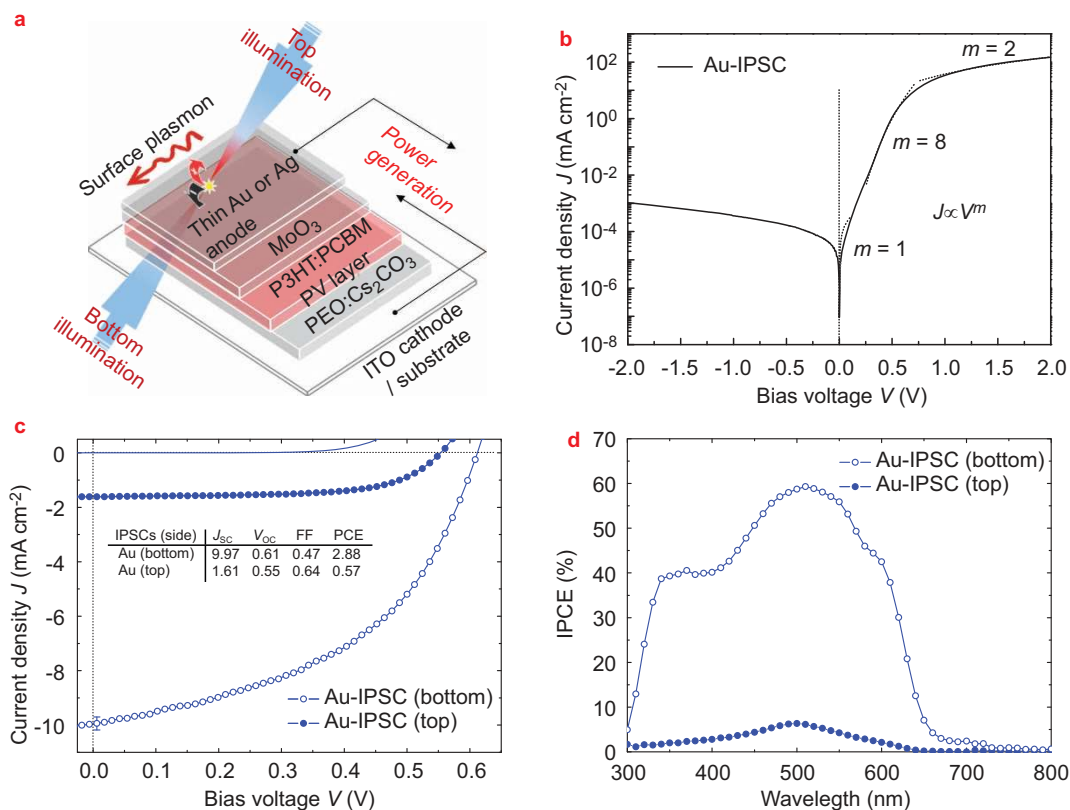
**Figure 1** (**a**) Schematic structure of the semitransparent inverted PV devices (Au- and Ag-IPSC). (**b**) Semilogarithmic plot of the dark *J–V* curve of an Au-IPSC. (**c**) *J–V* curve of the Au-IPSC under bottom illumination (open symbols), together with the curve under top illumination (closed symbols). (**d**) IPCE spectral curve of the Au-IPSC under bottom illumination (open symbols), together with the curve under top illumination (closed symbols). FF, fill factor; IPCE, incident photon-to-current collection efficiency; IPSC, inverted polymer solar cell; PCE, power conversion efficiency; PV, photovoltaic.

P3HT (band edge: approximately 650 nm) in the P3HT:PCBM PV layer used for the IPSC (Supplementary Fig. S1b and S1c). The Au-IPSC shows low transmission at wavelengths longer than the absorption edge (approximately 650 nm) of the P3HT:PCBM layer, mainly due to the strong optical reflection of the Au anode used for the IPSC (Supplementary Fig. S1c). These optical characteristics of the Au-IPSC were found to be similar to those of semitransparent IPSCs with a thin Ag anode (Ag-IPSC), although the transmission and reflection spectra differ between the Au and the Ag films (Supplementary Fig. S1c).

To gain further insight into the interaction between SPs and incident light in semitransparent IPSCs, we investigated the optical dispersion relationships for the multilayered material systems in the IPSCs by means of finite difference time domain (FDTD) calculations.[39,40] In the FDTD calculations, we used the complex refractive indices of the multilayers in the IPSCs, as determined by spectroscopic ellipsometric[25,41,42] and ATR prism-coupling[4–6] techniques, as the input parameters (Supplementary Fig. S2). Using the optical parameters of each functional layer at an appropriate thickness, such as the optimal Au thickness of approximately 45 nm (Supplementary Fig. S3) in IPSCs, we determined the dispersion relationships and found that the semitransparent IPSC structure under investigation clearly supports two TM-polarized resonant modes, arising from the strong coupling of the incident photons with the SPs at the two metal/dielectric interfaces, i.e., the metal anode-air (SP1 mode) and metal anode/(MoO$_3$)/PV (SP2 mode) interfaces (Supplementary Fig. S4).

We then investigated the current density–voltage (*J–V*) characteristics of the fabricated semitransparent IPSCs (Au- and Ag-IPSC).

Figure 1b shows the dark *J–V* characteristics of the fabricated semitransparent Au-IPSC, revealing good diodic behavior with high rectification ratios of $10^4$–$10^5$ at 2.0 V. Figure 1c shows the photo *J–V* characteristics of the IPSCs. Under bottom illumination, the Au-IPSC gave a good PV performance with an open-circuit voltage ($V_{OC}$) of 0.61 V, a short-circuit current density ($J_{SC}$) of 9.97 mA cm$^{-2}$ and a fill factor (FF) of 0.47. These results correspond to a PCE of approximately 2.9%, which is slightly higher than those (approximately 2.0%–2.5%) of similar devices reported elsewhere.[31] Under top illumination, however, the sample devices gave a relatively poor PV performance (PCE=0.57%), which is mainly attributed to the decreased intensity of light transmitted through the metal anodes. The PV performance of the studied devices is consistent with their IPCE spectra (Figure 1d). It is noteworthy that the absorption spectrum of the PV layer (Supplementary Fig. S1b) is responsible for the IPCE spectral shapes under bottom illumination, while the transmission spectrum of the thin metal anode is responsible for the IPCE spectral shapes under top illumination. It was also noted that the Ag-IPSC exhibits similar PV performance (Supplementary Fig. S5).

Next, we investigated the optical power absorbed by the multilayers in the Au-IPSC from incident light by means of FDTD simulations (Supplementary Fig. S6). We found that for incident light with a wavelength $\lambda$=633 nm, which corresponds to the wavelength just above the bandgap of the PV layer, the power absorption of the Au-IPSC most likely has two main contributors: PV absorption and SP excitation at $\theta=\theta_R$ for TM-polarized excitation light. However, for incident light of $\lambda$=500 nm, which corresponds to the wavelength of

maximum absorbance of the PV layer, most of the incident light is absorbed directly into the PV layer, implying a very small contribution of SP, even for TM-polarization. In contrast, for incident light of $\lambda=750$ nm, which corresponds to the wavelength just below the bandgap of the PV layer, most of the incident light is reflected at $\theta<\theta_R$ due to the high real and small imaginary refractive indices of the PV layer on the highly reflective Au anode. Alternatively, the light is absorbed by the Au anode layer when $\theta\approx\theta_R$ (only for TM-polarized light), with a small amount of absorption by the PV layer. Thus, it is clear that incident light with a wavelength of 633 nm is the most appropriate for the simultaneous observation of SPR excitation and the PV effect.

We then explored the excitation of SPs in semitransparent IPSCs using an ATR technique.[5,6] We used an ATR sample consisting of an Au-IPSC assembled with a coupling prism (Au-IPSC/prism) oriented in the Kretschmann geometry[4–6] (Figure 2a) to match the tangential (to the interface) component ($k_X$) of the wavevector of the incident light with wavelength $\lambda$ in the relatively high index ($n_0$) prism to the real part of the SP wavevector ($k_{SP}$), i.e.,

$$k_X = \frac{2\pi}{\lambda} n_0 \sin\theta_R = \mathrm{Re}(k_{SP}) \cong \left(\frac{2\pi}{\lambda}\right)\left(\frac{\varepsilon\varepsilon_M}{\varepsilon+\varepsilon_M}\right)^{0.5}$$

where $\varepsilon$ and $\varepsilon_M$ are the dielectric functions of the adjacent medium and metal, respectively.[4–6] We then measured the reflectance ($R$) from the Au-IPSC/prism as a function of $\theta$ for TM-polarized incident light. As shown in Figure 2b, for incident light of $\lambda=632.8$ nm, and above $\theta_C$ (41.7°), $R(\theta)$ shows a sudden decrease that falls almost to zero (resonance dip) at $\theta=43.8°$, which corresponds to $\theta_R$ of the SP1 mode on the Au/air interface. Two theoretical ATR spectra, based on the Fresnel

formulas[5,6] and the FDTD simulation,[39,40] are also shown in Figure 2b; these are almost identical and are in excellent agreement with the experimental results. In the TIR region just beyond $\theta_C$, the low $R$ of approximately 0.33 for the Au-IPSC/prism may mainly be attributed to the light-absorbing property of the P3HT:PCBM PV layer at $\lambda=632.8$ nm, which is just above the optical absorption edge of P3HT. To confirm this, Figure 2b also shows that the $R(\theta)$ spectra for the 594- and 532-nm excitations are significantly lower than those for the 632.8-nm excitation, because the excitation values are closer to the wavelength of maximum absorption of P3HT.

We also calculated the distribution of the electric field intensity ($|E|^2$) as functions of $\theta$ and depth $z$ (Figure 2c). The results show that the excitation of the SP1 mode at the Au/air interface for an incident wavelength of $\lambda=632.8$ nm is associated with a higher intensity in the air with deeper penetration than that achieved for incident light of $\lambda=594$ and 532 nm. These results clearly show that the photoexcitation just above the optical absorption edge (approximately 650 nm) of the P3HT:PCBM PV layer can generate strong SP fields on the Au anode in the IPSC. We also monitored the angular dependence of the PV performance of the Au-IPSC/prism, as shown in Figure 2d. The $J$–$V$ characteristics were observed under illumination by TM-polarized monochromatic light ($\lambda=632.8$ nm, 0.35 mW cm$^{-2}$) at three different incident angles (Figure 2e). At $\theta=42.0°$, just above $\theta_C$ (in the lower off-resonance region), the $J$–$V$ curve shows typical PV device characteristics with $V_{OC}=0.28$ V and $J_{SC}=3.88\times10^{-2}$ mA cm$^{-2}$, which are similar to those at $\theta=48.0°$ (in the higher off-resonance region). This $J_{SC}$ gives a conversion efficiency (electron/photon) of approximately 22%, which is close to the IPCE value of 21% at 632.8 nm (Figure 1d). At $\theta=\theta_R$
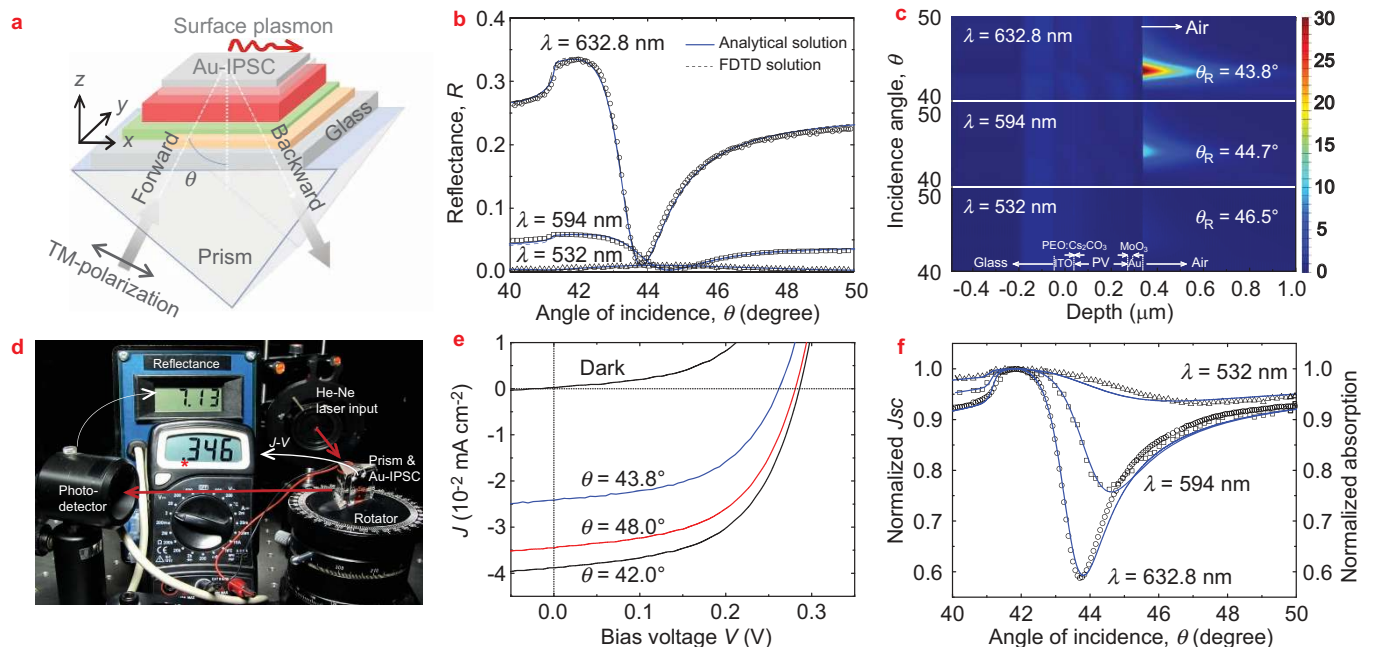


**Figure 2** (**a**) Schematic illustration of an Au-IPSC/prism under the Kretschmann configuration. (**b**) TM-polarized $R(\theta)$ of an Au-IPSC/prism for three incident lights ($\lambda=632.8$ nm, 594 nm and 532 nm). The curves represent two theoretical simulations of the Fresnel analytical model and the FDTD calculation, respectively. (**c**) Simulated depth profiles of electric field intensity ($|E|^2$) in the Au-IPSC structure as functions of $\theta$ and depth $z$ for incident wavelengths of $\lambda=632.8$ nm (upper), 594 nm (middle) and 532 nm (lower). (**d**) Photograph of an Au-IPSC/prism in operation mounted on a rotation stage to control $\theta$ of the incident light ($\lambda=632.8$ nm). By absorbing the incident light, the Au-IPSC generates electricity (*), enabling the simultaneous measurement of the $J$–$V$ characteristics, in addition to $R(\theta)$. (**e**) Measured $J$–$V$ curves of the Au-IPSC/prism at the resonance angle ($\theta=43.8°$), together with curves at the lower off-resonance ($\theta=42.0°$) and higher off-resonance ($\theta=48.0°$) regions for light illumination ($\lambda=632.8$ nm, 0.35 mW cm$^{-2}$). (**f**) Dependence of normalized $J_{SC}$ on $\theta$ for the Au-IPSC/prism based on the excitation wavelengths of 632.8 nm, 594 nm and 532 nm. The solid curves represent the simulated optical absorption of the P3HT:PCBM layer. FDTD, finite difference time domain; IPSC, inverted polymer solar cell; ITO, indium tin oxide; PCBM, phenyl C$_{61}$-butyric acid methyl ester; PEO, poly(ethylene oxide); P3HT, poly(3-hexylthiophene); TM, transverse-magnetic.

(43.8°); however, $J_{SC}$ decreases significantly to $3.10 \times 10^{-2}$ mA cm$^{-2}$, while $V_{OC}$ tends to decrease only slightly to 0.26 V. This significant decrease in $J_{SC}$ at this SPR angle, i.e., APG is thought to arise from the decreased optical absorption of the PV layer due to significantly attenuated reflectance from the Au anode *via* the excitation of the SPs. In other words, at this SPR angle, the forward-propagating light through the PV layer only contributes to the generation of photocurrents, because of the greatly attenuated backward-propagating light reflected from the anode, affording just above half (approximately 60%) its maximum $J_{SC}$ value.

We then observed the dependence of $J_{SC}$ of the Au-IPSC/prism on the incident angle (APG curves, Figure 2f) for TM-polarized incident light of $\lambda = 632.8$ nm. From the normalized $J_{SC}(\theta)$ curves shown in the figure, it is clear that when $\theta$ increases above $\theta_C$, $J_{SC}$ shows a pronounced dip at $\theta = \theta_R$. For transverse-electric-polarized (TE-polarized) incident light, however, $J_{SC}$ (approximately $3.90 \times 10^{-2}$ mA cm$^{-2}$) tends to decrease only slightly as $\theta$ increases (not shown). The behaviors of the $J_{SC}(\theta)$ curves are similar to those of the $R(\theta)$ spectra, except that the minimum value at the resonance dip of $J_{SC}$ always exceeds half its maximum value. To explain the behaviors of $J_{SC}(\theta)$, we simulated the normalized optical absorption of the PV layer. As shown in Figure 2f, the simulated optical absorption curve is in good agreement with the measured $J_{SC}(\theta)$ curve, confirming that the reduced absorption of the PV layer due to the excitation of SPs is the origin of the sharp dip (APG) in the $J_{SC}(\theta)$ curve. For incident wavelengths of $\lambda = 594$ and 532 nm, the normalized $J_{SC}$ curves broaden because of

their strong absorptions for forward-propagating incident light into the PV layer. This result shows that the optical excitation just above the absorption edge of the PV layer allows the sensitive monitoring of the excitation of SPs in terms of $J_{SC}$.

We also investigated the ATR and APG spectra of the Ag-IPSC (Supplementary Fig. S7), finding results similar to those of the Au-IPSC, i.e., the SPR dip angle of APG spectra is nearly identical to that of the ATR spectra, provided that our IPSCs were SPR-sensitive PV devices, acting like an optical detector integrated into an SPR coupler. Hereafter, we discuss the more stable Au anode in our IPSCs investigations (Supplementary Fig. S8).

Next, we investigated changes in the excitation of SPs on the IPSCs, induced by the introduction of nanoscale adlayers to the IPSCs, because SPR on a metal surface is highly sensitive to the adsorbed layer.[10,11] In this study, we used the fluoropolymer Cytop and a protein of BSA, one of the first subjects used in previous quantitative protein adsorption studies,[43] as adsorbates on the Au metal anode. Figure 3a shows the changes in $R(\theta)$ and $J_{SC}(\theta)$ spectra for the formation of the bi-adlayers of Cytop and BSA on an Au anode (Au anode/Cytop/BSA, left-hand panel) and for the desorption of the bi-adlayers by successive cleaning processes (right-hand panel). Note that the clear shift in the SPR dip angle after the formation of the upper BSA adlayer on the Cytop adlayer indicates that the BSA forms a well-defined adlayer with a good adsorption capacity on the hydrophobic Cytop surface. We also noted that the $R(\theta)$ and $J_{SC}(\theta)$ spectra were shifted to nearly identical angles for each step in the formation/
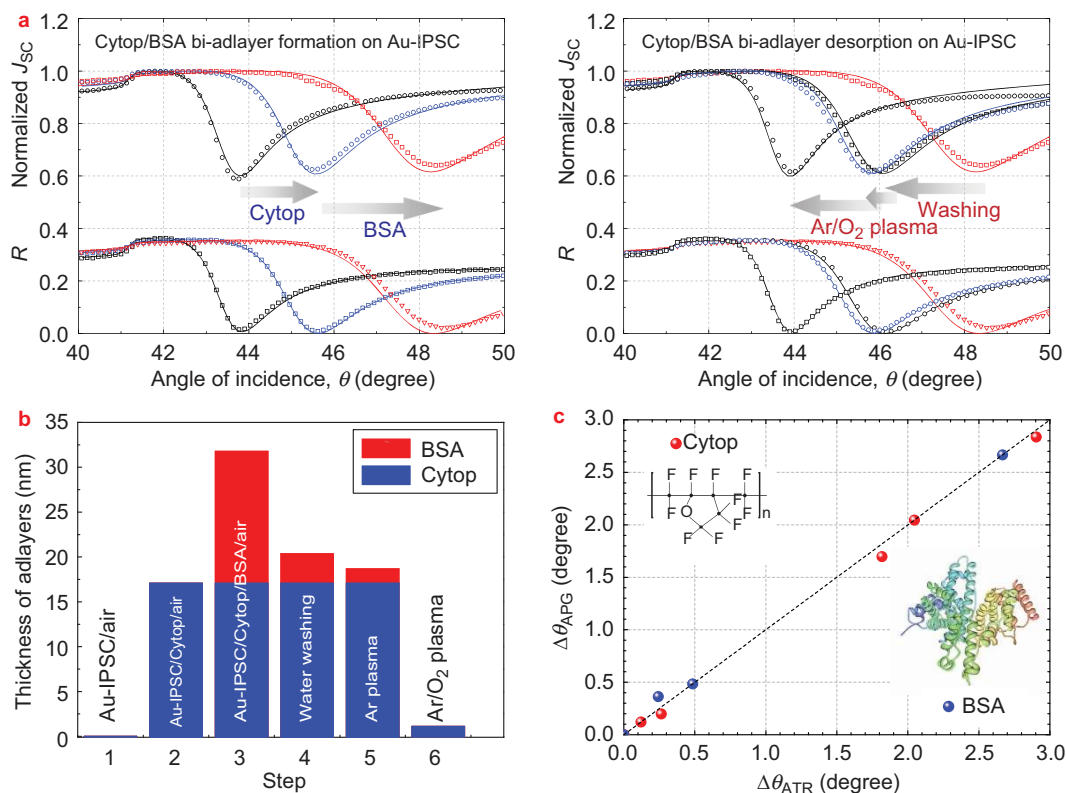


**Figure 3** (**a**) Changes in the $R(\theta)$ and $J_{SC}(\theta)$ spectra for the formation of the bi-adlayers of Cytop and BSA on an Au anode (Au anode/Cytop/BSA, left-hand panel) and for the desorption of the bi-adlayers by successive cleaning processes (right-hand panel). The simulated results are also shown as solid curves. (**b**) Estimated film thicknesses of the Cytop (blue bars) and the BSA (red bars) adlayers on Au-IPSC after each step in the formation/desorption processes. (**c**) Shifts in the SPR angles ($\Delta\theta_R$) in the $R(\theta)$ *versus* $\Delta\theta_R$ in the $J_{SC}(\theta)$, induced by changes in the adlayers of Cytop ($n=1.354$) and BSA ($n=1.502$). The dotted line represents the numerically calculated $\Delta\theta_R$ for an incident wavelength of $\lambda=632.8$ nm. Inset shows the molecular structures of Cytop and BSA. APG, attenuated photocurrent generation; ATR, attenuated total internal reflection; BSA, bovine serum albumin; IPSC, inverted polymer solar cell; SPR, surface plasmon resonance.

desorption processes, implying that the APG mode may potentially complement the ATR method. From the clear shift in the SPR excitation for each step, the thickness of each adlayer was estimated precisely by means of FDTD simulations.

Figure 3b shows the estimated film thicknesses of the Cytop (blue bars) and the BSA (red bars) adlayers on the Au-IPSC after each step of the formation/desorption processes (see also the atomic force microscopy results in Supplementary Fig. S9). Figure 3c shows a comparison of the shifts in $\theta_R$ ($\Delta\theta_R$) in $R(\theta)$ versus $\Delta\theta_R$ in $J_{SC}(\theta)$, induced by changes in the adlayers of Cytop and BSA on the Au-IPSC. Figure 3c also shows the numerically calculated values ($\Delta\theta_R$) in the $R(\theta)$ and $J_{SC}(\theta)$ (normalized optical absorption) spectra, induced by changing the thickness of the adlayers on the Au-IPSC. By comparison, it is clear that the $\Delta\theta_R$ values in $J_{SC}(\theta)$ are virtually identical to those in $R(\theta)$, revealing that not only ATR but also APG may be used as a sensitive and label-free SPR probe for the monitoring of nanoscale changes in the film thicknesses (or refractive indices) of adlayers. Moreover, the time-dependent changes in the ATR curves are almost identical to those in the APG curves, indicating that APG can be used in place of ATR to monitor changes in adlayers for analytes of interest *in situ* and in

real time (Supplementary Fig. S10). It is also noteworthy that the device performance of the Au-IPSC remained almost constant even after all of the formation/desorption processes, confirming the excellent performance stability of the Au-IPSC used (Supplementary Table S1).

To test the analyte-selective sensing of the APG responses systematically, we measured the variations in the SPR spectra due to biomolecular binding on the Au-IPSC; accordingly, we used the well-characterized specific biotin-STA interaction as a sensing model system. Figure 4a shows schematics for three different types of detection modes used to observe SPR spectra: conventional ATR (upper panel, Mode A) and APG (middle panel, Mode B) measurements with an ATR prism. For another APG detection mode with a lightguide geometry (lower panel, Mode C), index matching oil was used to attach the glass substrate of Au-IPSC to one end of a microscope glass slide, used as a lightguide medium, instead of the ATR prism. Mode C is based on the excitation of SPs by guided optical waves; therefore, at coupling angles above $\theta_C$, incident light is guided within the glass slide by TIR to the Au-IPSC. Figure 4b shows the observed SPR spectra corresponding to steps 1–3 for detection modes A–C with an incident wavelength of $\lambda = 632.8$ nm. As shown in the two upper SPR spectra measured using
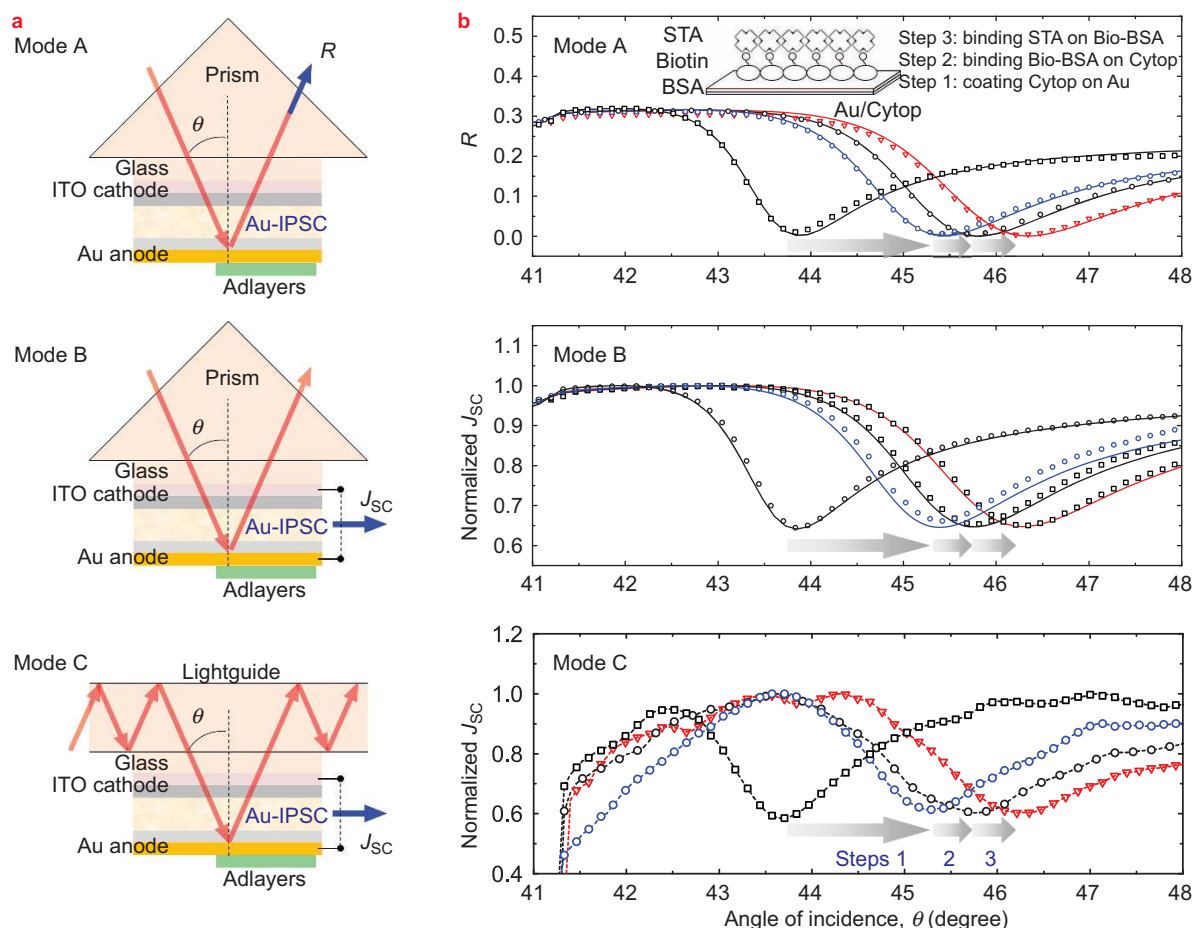


**Figure 4** (**a**) Schematics showing three types of detection modes for observing shifts in the SPR dips: $R(\theta)$ measurement with an ATR prism (upper, Mode A), $J(\theta)$ measurement with an ATR prism (middle, Mode B), and another $J(\theta)$ measurement with a planar lightguide (lower, Mode C). (**b**) SPR spectra corresponding to steps 1–3 of the molecular bindings for detection modes A (upper), B (middle) and C (lower). The simulated results are shown as solid curves. The inset shows a schematic diagram of the surface modification of the Au anode and the molecular bindings: the formation of adlayers of Cytop onto an Au anode surface (step 1), the formation of biotinylated BSA (Bio-BSA) on the Cytop surface (step 2) and STA binding to Bio-BSA *via* STA–biotin conjugation (step 3). ATR, attenuated total reflection; BSA, bovine serum albumin; IPSC, inverted polymer solar cell; ITO, indium tin oxide; SPR, surface plasmon resonance; STA, streptavidin.

the ATR prism, the SPR dips for Modes A and B are shifted to nearly identical angles after each step of the molecular binding process. At step 3 in particular, it was clearly confirmed that the specific binding of biomolecules of STA on the biotinylated Au-IPSC can be detected not only in the ATR mode but also in the APG mode. Moreover, even without the ATR prism, as shown in the lower spectral graph, using Mode C clear SPR dips can be observed, which also shifted to nearly the same angles as those in Modes A and B after each steps 1–3. Note that above $\theta_C$, at which point the sharp onset of $J_{SC}$ can be seen, the weak oscillatory behavior of $J_{SC}$ may be interpreted in terms of multiple reflections occurring in the active area of the Au-IPSC.

This result clearly demonstrates the effectiveness of Mode C, which can be applied to position-dependent sensing in space-confined environments, where mounting an ATR prism and/or external photodetector is difficult, and ATR cannot therefore be measured directly. Light propagation and detection in such a structure can easily be combined with other optical components, such as optical fibers or waveguides.

Finally, to estimate the dynamic ranges of the APG detection modes using Au-IPSC, we investigated the calibration curves for the changes in the SPR angles as a function of STA concentration at step 3, incubating the biotinyl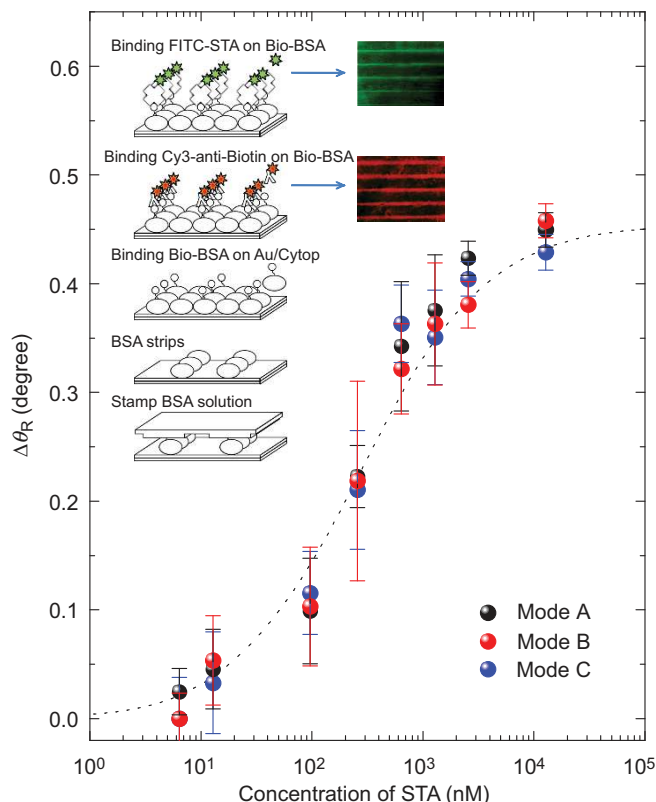ated Au-IPSC in solutions of STA (Figure 5). The results show the characteristic sigmoidal function of the STA concentration, and the data show a good fit to the Langmuir isotherm[44]

$$\Delta\theta_R = \Delta\theta_{R,MAX} \frac{K_a \cdot [STA]}{1 + K_a \cdot [STA]}$$

under the assumption that the shift in the SPR angle ($\Delta\theta_R$) due to the submonolayer coverage of STA reached a maximum ($\Delta\theta_{R,MAX}$) following the complete formation of the STA monolayer on the Bio-BSA. From the analysis, the association constants ($K_a$) between STA and surface-bound biotin for the APG modes (Modes B and C) are estimated to be approximately $3.5 \times 10^6$ $M^{-1}$, which is nearly identical to the value obtained from the ATR mode (Mode A). Moreover, the limits of detection of STA on Bio-BSA determined from the APG modes (Modes B and C) are found to be quite low (<7.5 nM) and practically identical to those obtained from the conventional ATR mode (Mode A).

The above results regarding APG detection modes provide clear justification for the use of an Au-IPSC to monitor SPRs sensitively in terms of $J_{SC}$ without the need for a complicated $\theta$–$2\theta$ scan, an ATR coupling prism, and/or an external photodetector. This APG mode also offers an additional advantage in the reduction of noise due to interference such as scattering, which could arise from turbid or strongly light-absorbing environments, unlike the ATR mode in which the reflected light beam from the SPR-coupling metal surface must travel through the environmental space to reach an external detector. Therefore, the use of an APG mode with an SPR-sensitive Au-IPSC, acting like an integrated SPR device, can facilitate the simple and real-time label-free detection of biological and chemical molecular species with high sensitivity.

## CONCLUSIONS

We have shown that the use of semitransparent inverted polymer PV devices with thin Au or Ag metal anodes allows the excitation of SPs on the anodes, resulting in the significant attenuation not only of TIR but also of photocurrent generation in the PV devices. We propose a mechanism to explain these observations based on the resonant light absorption of the SPR active anode in the polymer PV devices. We have also shown that biomolecular binding on the PV devices can lead to apparent shifts in the SPR angles in the APG and ATR spectra. The use of APG measurements in terms of $J_{SC}(\theta)$ may simplify and/or improve the conventional ATR configuration; thus, APG may be an efficient detection method for sensing analytes of interest, even in confined spaces. More importantly, we have highlighted the fact that APG results, together with the related PV properties described herein, also provide detailed insight into the characteristics of SP excitation in semitransparent inverted polymer PV devices. These results may guide the development of new compact, low-cost, high-performance and highly sensitive SPR-based optical devices.



**Figure 5** Quantitative label-free SPR response curves of STA binding isotherms on Bio-BSA (step 3) using the three detection modes A, B and C shown in Figure 4. The dotted curves show the best fit of the Langmuir isotherm. The inset shows label-based fluorescent images of the biomolecular binding, confirming the STA binding on a stripe-patterned Bio-BSA layer on the Au-IPSC. Red fluorescent anti-biotin-Cy3 monoclonal antibody and green fluorescent FITC-conjugated STA were used to visualize molecular binding on a stripe-patterned Bio-BSA layer. BSA, bovine serum albumin; FITC, fluorescein isothiocyanate; IPSC, inverted polymer solar cell; SPR, surface plasmon resonance; STA, streptavidin.

## AUTHOR CONTRIBUTIONS

BP contributed to the design of the study, analysis of the data and drafting of the manuscript. SHY, CYC, YCK, JCS, HGJ and YHH fabricated and characterized

## COMPETING FINANCIAL INTERESTS

The authors declare no competing financial interests.

1 Ritchie RH. Plasma losses by fast electrons in thin films. *Phys Rev* 1957; **106**: 874–881.

2 Ritchie RH, Arakawa ET, Cowan JJ, Hamm RN. Surface-plasmon resonance effect in grating diffraction. *Phys Rev Lett* 1968; **21**: 1530–1533.

3 Otto A. Excitation of nonradiative surface plasma waves in silver by the method of frustrated total reflection. *Z Phys* 1968; **216**: 398–410.

4 Kretschmann E. Die bestimmung optischer konstanten von metallen durch anregung von oberflächenplasmaschwingungen. *Z Phys* 1971; **241**: 313–324.

5 Raether H. *Excitation of Plasmons and Interband Transitions by Electrons*. Berlin: Springer; 1980.

6 Knoll W. Interfaces and thin films as seen by bound electromagnetic waves. *Annu Rev Phys Chem* 1998; **49**: 569–638.

7 Polman A. Plasmonics applied. *Science* 2008; **322**: 868–869.

8 Lindquist NC, Nagpal P, McPeak KM, Norris DJ, Oh SH. Engineering metallic nanostructures for plasmonics and nanophotonics. *Rep Prog Phys* 2012; **75**: 036501.

9 Fang Z, Zhu X. Plasmonics in nanostructures. *Adv Mater* 2013; **25**: 3840–3856.

10 Otte MA, Sepúlveda B, Ni W, Juste JP, Liz-Marzán LM *et al*. Identification of the optimal spectral region for plasmonic and nanoplasmonic sensing. *ACS Nano* 2010; **4**: 349–357.

11 Brolo AG. Plasmonics for future biosensors. *Nat Photon* 2012; **6**: 709–713.

12 Stuart HR, Hall DG. Absorption enhancement in silicon-on-insulator waveguides using metal island films. *Appl Phys Lett* 1996; **69**: 2327–2329.

13 Schaadt DM, Feng B, Yu ET. Enhanced semiconductor optical absorption *via* surface plasmon excitation in metal nanoparticles. *Appl Phys Lett* 2005; **86**: 063106.

14 Su YH, Ke YF, Cai SL, Yao QY. Surface plasmon resonance of layer-by-layer gold nanoparticles induced photoelectric current in environmentally-friendly plasmon-sensitized solar cell. *Light Sci Appl* 2012; **1**: e14; doi:10.1038/lsa.2012.14.

15 Polman A, Atwater HA. Photonic design principles for ultrahigh-efficiency photovoltaics. *Nat Mater* 2012; **11**: 174–177.

16 Hayashi S, Kozaru K, Yamamoto K. Enhancement of photoelectric conversion efficiency by surface plasmon excitation: a test with an organic solar cell. *Solid State Commun* 1991; **79**: 763–767.

17 Westphalen M, Kreibig U, Rostalski J, Lüth H, Meissner D. Metal cluster enhanced organic solar cells. *Sol Energy Mater Sol Cells* 2000; **61**: 97–105.

18 Kato K, Tsuruta H, Ebe T, Shinbo K, Kaneko F *et al*. Enhancement of optical absorption and photocurrents in solar cells of merocyanine Langmuir–Blodgett films utilizing surface plasmon excitations. *Mater Sci Eng C* 2002; **22**: 251–256.

19 Yamagishi K, Inoue J, Yamashita M. Surface plasmon resonance in organic photovoltaic cells with silver or gold electrodes. *Mol Cryst Liq Cryst* 2006; **462**: 83–90.

20 Mapel JK, Singh M, Baldo MA, Celebi K. Plasmonic excitation of organic double heterostructure solar cells. *Appl Phys Lett* 2007; **90**: 121102.

21 Sariciftci NS, Smilowitz L, Heeger AJ, Wudl F. Photoinduced electron transfer from a conducting polymer to buckminsterfullerene. *Science* 1992; **258**: 1474–1476.

22 Yu G, Gao J, Hummelen JC, Wudl F, Heeger AJ. Polymer photovoltaic cells: enhanced efficiencies *via* a network of internal donor-acceptor heterojunctions. *Science* 1995; **270**: 1789–1791.

23 Liang Y, Xu Z, Xia J, Tsai ST, Wu Y *et al*. For the bright future—bulk heterojunction polymer solar cells with power conversion efficiency of 7.4%. *Adv Mater* 2010; **22**: E135–E138.

24 You J, Dou L, Yoshimura K, Kato T, Ohya K *et al*. A polymer tandem solar cell with 10.6% power conversion efficiency. *Nat Commun* 2013; **4**: 1446.

25 Dennler G, Forberich K, Scharber MC, Brabec CJ, Tomiš I *et al*. Angle dependence of external and internal quantum efficiencies in bulk-heterojunction organic solar cells. *J Appl Phys* 2007; **102**: 054516.

26 Şahin Y, Alem S, de Bettignies R, Nunzi JM. Development of air stable polymer solar cells using an inverted gold on top anode structure. *Thin Solid Films* 2005; **476**: 340–343.

27 Li G, Chu CW, Shrotriya V, Huang J, Yang Y. Efficient inverted polymer solar cells. *Appl Phys Lett* 2006; **88**: 253503.

28 Small CE, Chen S, Subbiah J, Amb CM, Tsang SW *et al*. High-efficiency inverted dithienogermole–thienopyrrolodione-based polymer solar cells. *Nat Photon* 2012; **6**: 115–120.

29 He Z, Zhong C, Su S, Xu M, Wu H *et al*. Enhanced power-conversion efficiency in polymer solar cells using an inverted device structure. *Nat Photon* 2012; **6**: 591–595.

30 Park B, Shin JC, Cho CY. Water-processable electron-collecting layers of a hybrid poly(ethylene oxide): caesium carbonate composite for flexible inverted polymer solar cells. *Sol Energy Mater Sol Cells* 2013; **108**: 1–8.

31 Tao C, Ruan S, Zhang X, Xie G, Shen L *et al*. Performance improvement of inverted polymer solar cells with different top electrodes by introducing a MoO$_3$ buffer layer. *Appl Phys Lett* 2008; **93**: 193307.

32 Tvingstedt K, Persson NK, Inganäs O, Rahachou A, Zozoulenko IV. Surface plasmon increase absorption in polymer photovoltaic cells. *Appl Phys Lett* 2007; **91**: 113514.

33 Chang YC, Chou FY, Yeh PH, Chen HW, Chang SH *et al*. Effects of surface plasmon resonant scattering on the power conversion efficiency of organic thin-film solar cells. *J Vac Sci Technol B* 2007; **25**: 1899–1902.

34 Gan Q, Bartoli FJ, Kafafi ZH. Plasmonic-enhanced organic photovoltaics: breaking the 10% efficiency barrier. *Adv Mater* 2013; **25**: 2385–2396.

35 Stratakis E, Kymakis E. Nanoparticle-based plasmonic organic photovoltaic devices. *Mater Today* 2013; **16**: 133–146.

36 Kao CS, Chen FC, Liao CW, Huang MH, Hsu CS. Plasmonic-enhanced performance for polymer solar cells prepared with inverted structures. *Appl Phys Lett* 2012; **101**: 193902.

37 Li X, Choy WC, Huo L, Xie F, Sha WE *et al*. Dual plasmonic nanostructures for high performance inverted organic solar cells. *Adv Mater* 2012; **24**: 3046–3052.

38 Xu P, Shen L, Meng F, Zhang J, Xie W *et al*. The role of Ag nanoparticles in inverted polymer solar cells: surface plasmon resonance and backscattering centers. *Appl Phys Lett* 2013; **102**: 123301.

39 Yee KS. Numerical solution of initial boundary value problems involving maxwell's equations in isotropic media. *IEEE Trans Antenn Propag* 1966; **14**: 302–307.

40 *FDTD Solutions*. Vancouver: Lumerical Solutions Inc.

41 Woollam JA, Johs BD, Herzinger CM, Hilfiker JN, Synowicki RA *et al*. Overview of variable-angle spectroscopic ellipsometry (VASE): I. Basic theory and typical applications. *Proc SPIE* 1999; **CR72**: 3–28.

42 Johs BD, Woollam JA, Herzinger CM, Hilfiker JN, Synowicki RA *et al*. Overview of variable-angle spectroscopic ellipsometry (VASE): II. Advanced applications. *Proc SPIE* 1999; **CR72**: 29–58.

43 Bull HB. Adsorption of bovine serum albumin on glass. *Biochim Biophys Acta* 1956; **19**: 464–471.

44 Riboh JC, Haes AJ, McFarland AD, Yonzon CR, van Duyne RP. A nanoscale optical biosensor: real-time immunoassay in physiological buffer enabled by improved nanoparticle adhesion. *J Phys Chem B* 2003; **107**: 1772–1780.